eprints@whiterose.ac.uk
https://eprints.whiterose.ac.uk/

Novel Generic Fault Model Considering Fundamental and PWM Current Components of PM Machines with Inter-Turn Short-Circuit

Y. Qin, *Student Member, IEEE*, G. J. Li, *Senior Member, IEEE,* Z. Q. Zhu, *Fellow, IEEE,* M. P. Foster, D. A. Stone, C. J. Jia, and P. McKeever

Abstract— **This paper proposes a novel analytical fault model for permanent magnet machines with inter-turn short-circuits that considers the influence of various factors on the fault current. These factors include (1) mutual inductances between the faulted turns and the remaining healthy windings (faulted and healthy phases), (2) load current, and (3) PWM harmonics introduced by the drives. These three factors have been largely neglected by the published methods in literatures but could have significant influence on fault current depending on operating conditions. The investigation in this article shows that, without using the proposed fault model, the conventional fault model that only considers the back-EMF in the short-circuited loop and the self-impedance of the short-circuited turns, would underestimate the fundamental fault current by more than 45%. In addition, the proposed model establishes the relationship between the PWM ripple current in the short-circuited turns and that in the faulted phase. By doing so, the fault current including both the fundamental and PWM ripple components can be accurately predicted. The accuracy of the proposed method has been fully validated by a series of experiments.**

Index Terms— **Fault current, fault modelling, inter-turn short-circuit fault, PM machine, PWM ripple current.**

I. INTRODUCTION

INTER-turn short-circuit (ITSC) faults in the PM machines have attracted increasing attention due to their potential catastrophic consequences for the reliability of safety-critical applications such as aerospace and offshore wind power [1]. This serious fault is caused by the winding insulation failure resulting from the high rates of voltage change (*dv/dt*) [2], thermal stress or environmental contamination [3] [4]. It is reported that the fault current in the short-circuited path can be many times (>30) higher than the rated current [3]. The extremely large fault current leads to local overheating of the short-circuited turns, which could lead to the meltdown of the entire phase and eventually result in a permanent damage to the machines. Given the potential risk posed by the ITSC fault, fault detection methods and post-fault remedial control strategies are often required to prevent a local fault from escalating into a more severe system-level fault [5] [6] [7]. However, fault modelling has often been deemed critical as it helps to develop effective model-based fault detection and mitigation methods [8], [9]. Accurate fault model can be used to predict the electromagnetic performances especially the fault current under ITSC faults. This can provide theoretical support needed for designing the machine parameters, e.g., phase inductance and resistance, and phase back-EMF, etc., to achieve desired fault tolerant capability [10]. For the fault current, its amplitude or Root Mean Square (RMS) value is

regarded as the key parameter. This is because, once these two parameters are obtained, they can be used to calculate copper loss (main heat source) in faulty turns, and hence to predict the temperature rise after ITSC fault [11]. In addition, the magnitude of the fault current provides insight into the severity of the fault and its potential impact on machine performance and reliability [12].

To simplify the analysis of fault current, it is often assumed that the back-EMF in the short-circuited path plays a dominant role in fault current prediction. As a result, the fault current can be simplified as equal to the back-EMF in the short-circuited path divided by the self-impedance of the faulted turns [13] [14] [15]. However, this approach does not consider the effect of the mutual inductances between the faulty turns and the remaining healthy windings (both faulty and healthy phases) on the fault current. In [16], single-layer PMSM is investigated, where the mutual inductances between phases have been ignored. Only the mutual inductance between the faulted turns and the remaining healthy winding of the faulted phase has been considered. As a result, the fault current will only be influenced by the back-EMF and faulted phase current. In order to obtain the amplitude of the fault current, this paper makes some assumptions, setting the load currents to be zero. If so, the fault current will be only affected by the back EMF of the faulted turns. From the perspective of determining the amplitude of fault current, this approach is the same as those proposed in [13] [14] [15]. In [10] and [17], the fault current expression for a PM machine with fractional slot concentrated windings (FSCW) is presented taking the mutual inductance between the short-circuited turns and the remaining healthy winding of the faulted phase into consideration. However, the mutual inductances between the short-circuited turns and the healthy phases have been neglected due to the negligible mutual flux between phases. As a result, this approach is limited to the specific case studied and cannot be applied to machines with large mutual inductances. In [18], a more generic fault current model considering all the above-mentioned mutual inductances has been developed. However, it neglected the effect of flux-weakening control strategy, which can reduce the total flux in the short-circuited path and thus reduce the fault current. An improved fault current expression considering the flux-weakening control strategy has been presented in [19], in which it indicated that the phase current and the back-EMF in the short-circuited path jointly contribute to the fault current. However, this approach can only analyze the change of fault current qualitatively. If the number of short-circuited turns is

changed or the flux-weakening control strategy is adopted, the amplitude or the RMS value of fault current cannot be predicted quantitatively. In [20], despite the full consideration of all aforementioned mutual inductances, the amplitudes of the fault current achieved depend on the access to the faulted phase voltage. Consequently, it requires the addition of voltage sensors and access to the neutral point, thereby increasing hardware costs and escalating system complexity. As a result, these factors impose limitations on its widespread adoption. It is worth noting that all the above methods for predicting fault currents ignore the PWM harmonics. However, the fault current actually contains a large amount of PWM harmonics, especially in the case where a few turns are short-circuited [21]. In [21], a novel fault model has been proposed to account for the effect of the drive, which takes into account the PWM harmonics in the fault current. However, it cannot derive an analytical expression for the fault current. Therefore, it cannot quantitatively predict the amplitudes (or RMS values) of the fundamental and PWM components of the fault current.

To overcome these limitations, this article aims to develop a generic fault model, i.e., an analytical expression, for directly predicting the amplitude or RMS value of the fault current. This model considers various factors such as (1) mutual inductances between the faulty turns and the remaining healthy windings (both faulty and healthy phases), (2) load current, and (3) PWM harmonics introduced by the drives. Despite their potential significant impact on the fault current depending on the operating conditions, most the existing methods in the literature largely ignore these factors. The investigation in this article reveals that the conventional fault model, which considers only the back-EMF in the short-circuited loop and the self-impedance of the short-circuited turns, could underestimate the fundamental fault current by more than 45%. However, this underestimation can be avoided by adopting the proposed fault model. In addition, this paper establishes the correlation between the PWM ripple current in the short-circuited turns and in the faulted phase. This makes it possible to accurately predict the fault current including the fundamental and the PWM ripple components. This topic has received little attention in the literature, making it the primary novelty and contribution of this paper.

II. ANALYTICAL MODEL OF MACHINES WITH ITSC

A. Development of the Fault Model

A schematic of a typical 3-phase PWM inverter-fed PM machine is shown in Fig. 1. The parameters for this investigated machine are listed in TABLE I. Here, the output voltages from the inverter, labeled as V_{dslA}, V_{dslB} and V_{dslC}, are the inputs to the PM machine, and the currents (i_a, i_b, i_c and i_f) are the machine output signals. In this paper, it is assumed that thick cables with negligible resistance are used to connect the inverter and the
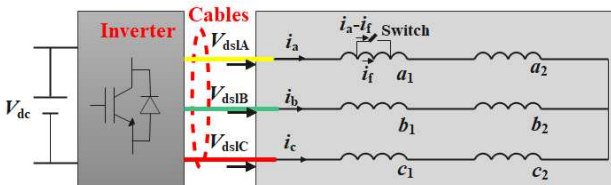

Fig. 1 PMSM with series connected coils under ITSC fault in phase A.

TABLE I PARAMETERS OF PM MACHINE WITH ITSC FAULTS

Nº of phases	3	Phase resistance (mΩ)	446
Nº of poles/slots	8/6	Phase inductance (μH)	270
Nº of turns per coil	24	PM flux (mWb)	5.944
Maximum power	200 W	Maximum Torque	1.27 Nm
Maximum speed	1500 rpm	Maximum current	15 A

PM machine. So, the influence of the cable resistances on the fault model can be neglected. Moreover, each machine winding consists of two coils in series, and it is assumed that the ITSC fault occurs at the coil a_1, as shown in Fig. 1.

It is worth noting that this paper only pays attention to the full short-circuit stage, where the contact resistance of the ITSC is 0Ω. This is because the fault current generated at this stage is much larger than that at the incipient fault stage. According to Kirchhoff's voltage law (KVL), the relationship between the input voltages (V_{dslA}, V_{dslB} and V_{dslC}) and the output currents (i_a, i_b, i_c and i_f) can be described by (1), where v_n is the zero-sequence voltage. Since the sum of the three-phase currents is equal to zero, v_n in (1) can be further deduced as (3). The zero sequence voltage under ITSC fault is different from that at healthy condition, which could be used as a fault indicator for fault detection [22]. Although the machine with two coils in series is taken as an example, the developed fault model can also be extended to other different numbers of coils in series. To do so, only the R and L matrices in (2) need to be updated.

$$L\frac{d}{dt}\begin{bmatrix} i_a \\ i_b \\ i_c \\ i_f \end{bmatrix} = -R\begin{bmatrix} i_a \\ i_b \\ i_c \\ i_f \end{bmatrix} + \begin{bmatrix} v_{Adsl} \\ v_{Bdsl} \\ v_{Cdsl} \\ 0 \end{bmatrix} - \begin{bmatrix} e_{ah} \\ e_b \\ e_c \\ e_{af} \end{bmatrix} - \begin{bmatrix} 1 \\ 1 \\ 1 \\ 0 \end{bmatrix} v_n \quad (1)$$

with

$$R = \begin{bmatrix} R_{s11} & 0 & 0 & 0 \\ 0 & R_{s22} & 0 & 0 \\ 0 & 0 & R_{s33} & 0 \\ 0 & 0 & 0 & R_{s44} \end{bmatrix} \text{ and } L = \begin{bmatrix} L_{s11} & M_{s12} & M_{s13} & M_{s14} \\ M_{s21} & L_{s22} & M_{s23} & M_{s24} \\ M_{s31} & M_{s32} & L_{s33} & M_{s34} \\ M_{s41} & M_{s42} & M_{s43} & L_{s44} \end{bmatrix}$$

(2)

$$v_n = -\frac{1}{3}\begin{bmatrix} 1 \\ 1 \\ 1 \\ 0 \end{bmatrix}^T \left\{ L\frac{d}{dt}\begin{bmatrix} i_a \\ i_b \\ i_c \\ i_f \end{bmatrix} + R\begin{bmatrix} i_a \\ i_b \\ i_c \\ i_f \end{bmatrix} - \begin{bmatrix} v_{Adsl} \\ v_{Bdsl} \\ v_{Cdsl} \\ 0 \end{bmatrix} + \begin{bmatrix} e_{ah} \\ e_b \\ e_c \\ e_{af} \end{bmatrix} \right\} \quad (3)$$

where R is the resistance matrix and L is the inductance matrix, and both matrices have a dimension of 4×4. R_{s11} is the resistance of the remaining healthy winding of phase A and R_{s44} is the resistance of the faulty turns. R_{s22} and R_{s33} are the resistances of phase B and phase C. e_{ah} and e_{af} represent the back-EMF of the healthy and faulty turns in phase A, e_a, e_b and e_c represent the back-EMFs of phases A, B and C, respectively. L_{s11} and L_{s44} are the inductances of the healthy and faulty turns in phase A, L_{s22} and L_{s33} represent the total self-inductances of phases B and C, respectively. M_{s12} and M_{s21} are the mutual inductances between the healthy winding of phase A and phase B, M_{s13} and M_{s31} are the mutual inductances between the healthy winding of phase A and phase C, and M_{s14} and M_{s41} are the mutual inductances between the healthy winding and faulty winding of phase A. M_{s23} and M_{s32} are the mutual inductances between phase B and phase C. M_{s24} and M_{s42} are the mutual inductances between phase B and faulty windings of phase A, while M_{s34} and M_{s43} are the mutual inductances between phase C and faulty winding of phase A. It is of significance to

highlight that, utilizing the parameters listed in TABLE I and accounting for the fault ratio (x), one can derive the components comprising matrices $\mathbf{L}$ and $\mathbf{R}$ according to the work presented in [18].

By replacing v_n in (1) using (3), (1) can be further derived as (4). Since the rank of the matrix $\mathbf{P}$ is equal to 3, and less than its dimension of 4, the matrix $\mathbf{P}$ is known as a singular matrix. As a result, it is impossible to solve (4) to achieve a unique solution for the currents. To solve this problem, new voltages and currents are constructed to reduce the order of system. More details can be seen in APPENDIX A.

$$\mathbf{PL}\frac{d}{dt}\begin{bmatrix} i_a \\ i_b \\ i_c \\ i_f \end{bmatrix} = -\mathbf{PR}\begin{bmatrix} i_a \\ i_b \\ i_c \\ i_f \end{bmatrix} + \mathbf{P}\begin{bmatrix} v_{Adsl} \\ v_{Bdsl} \\ v_{Cdsl} \\ 0 \end{bmatrix} - \mathbf{P}\begin{bmatrix} e_{ah} \\ e_b \\ e_c \\ e_{af} \end{bmatrix} \quad (4)$$

with

$$\mathbf{P} = \frac{1}{3}\begin{bmatrix} 2 & -1 & -1 & 0 \\ -1 & 2 & -1 & 0 \\ -1 & -1 & 2 & 0 \\ 0 & 0 & 0 & 3 \end{bmatrix} \text{ and } \begin{bmatrix} e_{ah} \\ e_b \\ e_c \\ e_{af} \end{bmatrix} = \begin{bmatrix} 1-\frac{1}{2}x & 0 & 0 \\ 0 & 1 & 0 \\ 0 & 0 & 1 \\ \frac{1}{2}x & 0 & 0 \end{bmatrix}\begin{bmatrix} e_a \\ e_b \\ e_c \end{bmatrix} \quad (5)$$

where $x = N_{fault}/N$ is faulty turn ratio of coil a_1, and N_{fault} and N are the number of faulty turns and the total number of turns respectively.

It can be observed from (A4) and (A5) that the order of the system can be successfully reduced by one due to $i_0 = 0$. With (A4) and (A5), (1) can be finally established as (6) in α- and β- axis reference frame. Since the order of the system is reduced from 4 to 3, the simplified fault model in α- and β-axis reference frame is beneficial to further explore the characteristics of fault current, as will be explained in section III.

$$\frac{d}{dt}[i_{\alpha\beta f}] = [L_{3\times3}^{-1} \times R_{3\times3}][i_{\alpha\beta f}] + [L_{3\times3}^{-1}][v_{\alpha\beta f}] \quad (6)$$

where $i_{\alpha\beta f}$ represents the current matrix with a dimension of 3×1 and consists of i_α, i_β and i_f. Similarly, $v_{\alpha\beta f}$ represents the voltage matrix with a dimension of 3×1 and consists of v_α, v_β and v_f.

B. Validation for the Proposed Fault Model

To validate the proposed fault model, a test rig has been built, as depicted in Fig. 2. The test rig consists of three main
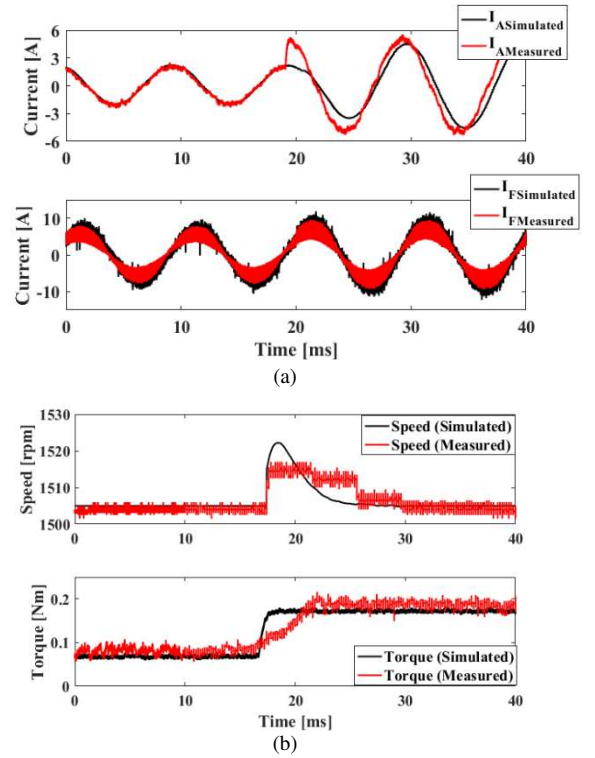

Fig. 3 (a) Simulated and measured faulted phase current (i_a) and fault current (i_f), and (b) simulated and measured speed and torque waveforms. Rotor speed is 1500 rpm and demand currents change from i_d =0 A and i_q = 2 A to i_d = 0 A and i_q = 5 A at around 20ms. The fault ratio is x=1/24.

components: the tested machine and dyno machine with associated DSP based voltage source inverters (VSI), couplings, and a torque meter. The test machine with ITSC faults, operates in torque mode, while the dyno machine operates in speed mode, providing a stable speed for the system. The torque meter is utilized for measuring the speed and torque. Fig. 2 shows that a thick wire was carefully selected and soldered to the faulted turn taps (coil a_1-faulted coil) to minimize its impedance in the short-circuited path. A switch (with negligible resistance) is employed to short-circuit the wire, emulating the ITSC fault. Furthermore, shows that the fault current (i_f) flowing through the faulty turns can be determined as the difference between i_a and (i_a-i_f), which can be directly measured using a current clamp. Encoders are mounted at the ends of both machines to measure
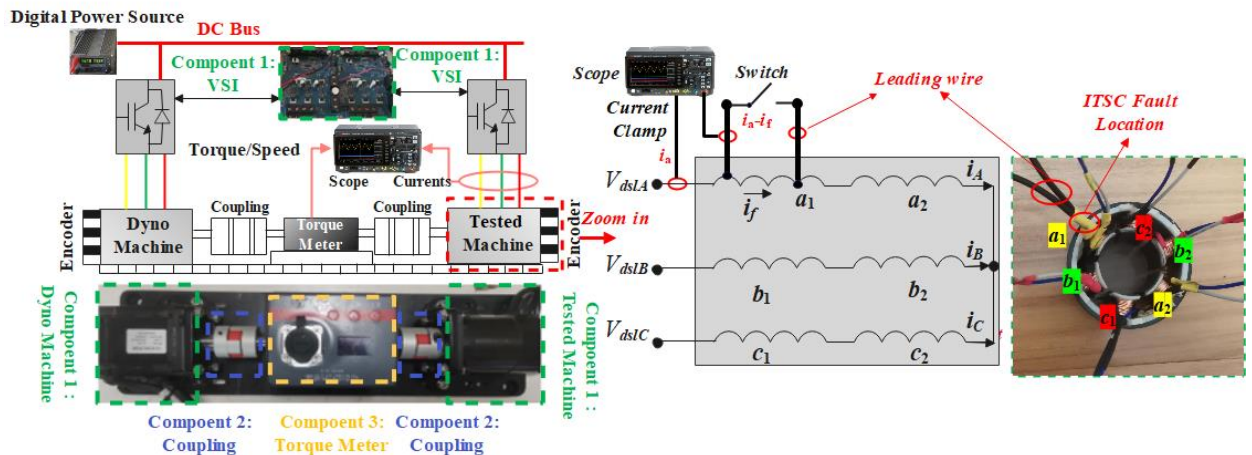

Fig. 2 Test setup with ITSC fault in the test PM machine.

the speed and position, which are crucial parameters for the field-oriented control (FOC) used in this paper. The test machine and dyno machine are independently controlled using two sets of three-phase inverters. Unless otherwise specified, the space vector pulse width modulation (SVPWM) strategy has been employed and the DC bus voltage, the dead time, and the switching frequency are set to 24V, 0.5μs, and 20kHz, respectively.

Simulated and measured results were compared, as shown in Fig. 3. It can be observed from Fig. 3 (a) that the simulated fault phase currents (i_a) both under steady and transient states match well with the measured ones. Similarly, the fault current (i_f) exhibits good agreement between simulation and measurement. The difference between simulated and measured speed and torque during transient state, i.e., during the load change at around 20 ms, as shown in Fig. 3 (b), is mainly due to the difference between the combined moment of inertia in the experiment and that in the simulation.

III. FAULT CURRENT INVESTIGATION

A. Investigation of Fundamental Component in Fault Current

As most existing literature, this section focuses on the fundamental component of the fault current. These currents can be considered sinusoidal if all harmonics in the currents are ignored. It is the same for the voltages (v_α, v_β and v_f). For a sinusoidal signal, its generic expression can be given as (7). Since K and θ are constants, F_s and F_c determined by K and θ, seen in (8), are deemed as constants as well. F_s and F_c for each sinusoidal signal in a first and multi-order system have been discussed in detail in APPENDIX B.

$$f(t) = Ksin(\omega t + \theta) = F_s \sin(\omega t) + F_c \cos(\omega t) = \begin{bmatrix} sin(\omega t) \\ cos(\omega t) \end{bmatrix}^T \begin{bmatrix} F_s \\ F_c \end{bmatrix}$$
(7)

with

$$F_s = K \cos\theta, F_c = K \sin\theta, \text{ and } K = \sqrt{F_s^2 + F_c^2}$$
(8)

where K and ω are the amplitude and frequency of the sinusoidal signal, respectively. θ is the initial phase angle.

Based on (B7) and (B8), (6) can be further expressed as (9).

$$\begin{bmatrix} i_{\alpha s} \\ i_{\alpha c} \\ i_{\beta s} \\ i_{\beta c} \\ i_{fs} \\ i_{fc} \end{bmatrix} = \begin{bmatrix} A_1 & B_1 & 0 & 0 & C_1 & D_1 \\ -B_1 & A_1 & 0 & 0 & -D_1 & C_1 \\ 0 & 0 & A_2 & B_2 & 0 & 0 \\ 0 & 0 & -B_2 & A_2 & 0 & 0 \\ A_3 & B_3 & 0 & 0 & C_2 & D_2 \\ -B_3 & A_3 & 0 & 0 & -D_2 & C_2 \end{bmatrix} \begin{bmatrix} v_{\alpha s} \\ v_{\alpha c} \\ v_{\beta s} \\ v_{\beta c} \\ v_{fs} \\ v_{fc} \end{bmatrix}$$
(9)

where $i_{\alpha s}$, $i_{\beta s}$ and i_{fs}, and $i_{\alpha c}$, $i_{\beta c}$ and i_{fc} are F_s and F_c of i_α, i_β and i_f, respectively. Similarly, $v_{\alpha s}$, $v_{\beta s}$ and v_{fs}, and $v_{\alpha c}$, $v_{\beta c}$ and v_{fc} are all F_s and F_c of the v_α, v_β and v_f, respectively. The elements in matrices $[L_{3\times3}^{-1} \times R_{3\times3}]$ and $[L_{3\times3}^{-1}]$ in (6) are determined by fault ratio (x), machine parameters such as phase inductance and resistance, which have been measured and given in TABLE I for this investigated PM machine. As a result, based on (6), (B7) and (B8), it can be concluded that A_1, B_1, A_2, B_2, A_3, B_3, C_1, D_1, C_2, and D_2 in (9) are functions of x and electrical angular speed (ω_e) of the machine, as seen from (B9) to (B19) in APPENDIX B.

Regarding the fundamental components, based on (9), the amplitudes of i_α, i_β and i_f can be presented as (10).

$$\begin{cases} \sqrt{(i_{\alpha s}^2 + i_{\alpha c}^2)} = \sqrt{\underbrace{K_{11}(v_{\alpha s}^2 + v_{\alpha c}^2)}_{1st} + \underbrace{2K_{12}(v_{\alpha s}v_{fs} + v_{\alpha c}v_{fc})}_{2nd} + \underbrace{2K_{13}(v_{\alpha s}v_{fc} - v_{\alpha c}v_{fs})}_{3rd} + \underbrace{K_{14}(v_{fs}^2 + v_{fc}^2)}_{4th}} \\ \sqrt{i_{\beta s}^2 + i_{\beta c}^2} = \sqrt{(A_2^2 + B_2^2)}\sqrt{(v_{\beta s}^2 + v_{\beta c}^2)} \\ \sqrt{i_{fs}^2 + i_{fc}^2} = \sqrt{\underbrace{K_{31}(v_{\alpha s}^2 + v_{\alpha c}^2)}_{1st} + \underbrace{2K_{32}(v_{\alpha s}v_{fs} + v_{\alpha c}v_{fc})}_{2nd} + \underbrace{2K_{33}(v_{\alpha s}v_{fc} - v_{\alpha c}v_{fs})}_{3rd} + \underbrace{K_{34}(v_{fs}^2 + v_{fc}^2)}_{4th}} \end{cases}$$
(10)

with

$$\begin{cases} K_{11} = A_1^2 + B_1^2, K_{12} = A_1C_1 + B_1D_1 \\ K_{13} = A_1D_1 - B_1C_1, K_{14} = C_1^2 + D_1^2 \\ K_{31} = A_3^2 + B_3^2, K_{32} = A_3C_3 + B_3D_3 \\ K_{33} = A_3D_3 - B_3C_3, K_{34} = C_3^2 + D_3^2 \end{cases}$$
(11)

It is found that the 2nd and 3rd terms are negligible compared to the 1st and 4th terms in (10). As a result, (10) can be simplified as (12).

$$\begin{cases} \sqrt{(i_{\alpha s}^2 + i_{\alpha c}^2)} = \sqrt{K_{11}(v_{\alpha s}^2 + v_{\alpha c}^2) + K_{14}(v_{fs}^2 + v_{fc}^2)} \\ \sqrt{i_{\beta s}^2 + i_{\beta c}^2} = \sqrt{(A_2^2 + B_2^2)}\sqrt{(v_{\beta s}^2 + v_{\beta c}^2)} \\ \sqrt{i_{fs}^2 + i_{fc}^2} = \sqrt{K_{31}(v_{\alpha s}^2 + v_{\alpha c}^2) + K_{34}(v_{fs}^2 + v_{fc}^2)} \end{cases}$$
(12)

It should be noticed from (12) that $\sqrt{(v_{fs}^2 + v_{fc}^2)}$ is actually the amplitude of the voltage (E_{af}) in the short-circuited turns, which can be further derived as (13). A coefficient 1/2 is used because each phase of the investigated machine has two series-connected coils. In addition, (13) has considered the impact of flux-weakening, which reduces the total flux in the short-circuited path, leading to reduced voltage.

$$\sqrt{(v_{fs}^2 + v_{fc}^2)} = E_{af} = \frac{1}{2}x(L_d i_d + \varphi_m)\omega_e$$
(13)

with

$$L_d = \left(\frac{x^2}{3} - \frac{2}{3}x + 1\right)L_l + \left(\frac{x^2}{3} - x + \frac{3}{2}\right)L_m$$
(14)

where L_d is the equivalent inductance of d-axis under the ITSC fault condition [17], i_d is the d-axis current, ω_e is the electrical angular speed of the machine and φ_m is the PM flux-linkage. L_m is the self-magnetizing inductance and L_l is the leakage inductance.

For the PM machine, with x and ω_e, and other parameters of the machine such as phase resistance, phase inductance, etc., K_{11}, K_{14}, K_{31} and K_{34} can be determined. In addition, if the load currents (i_d and i_q) are given, with the current closed loop control, the amplitude of i_α will be equal to $\sqrt{(i_d^2 + i_q^2)}$.

Finally, based on (12), (13) and (B2), the fault current can be derived as (15).

$$\sqrt{i_{fs}^2 + i_{fc}^2} = \sqrt{\underbrace{\frac{K_{31}}{K_{11}}\left(i_d^2 + i_q^2\right)}_{1st} + \underbrace{\frac{K_{11}K_{34} - K_{31}K_{14}}{K_{11}}\left(E_{af}^2\right)}_{2nd}}$$

(15)

Compared with the traditional fault current prediction method [13] [14] [15] [16], as seen in (16), this proposed method considers the impact of load current on the fault current. In addition, since K_{11}, K_{14}, K_{31} and K_{34} in (15) are derived from the fault model, all the mutual inductances have been considered, as seen in (2).

$$\sqrt{i_{fs}^2 + i_{fc}^2} = \frac{E_{af}}{\sqrt{R_{s44}^2 + (\omega_e L_{s44})^2}}$$

(16)

To rigorously assess the impact of influencing factors on fault current, including (1) mutual inductances between the faulted turns and the remaining healthy windings (faulted and healthy phases), (2) load current, and (3) PWM harmonics introduced by the drives, a comprehensive validation process
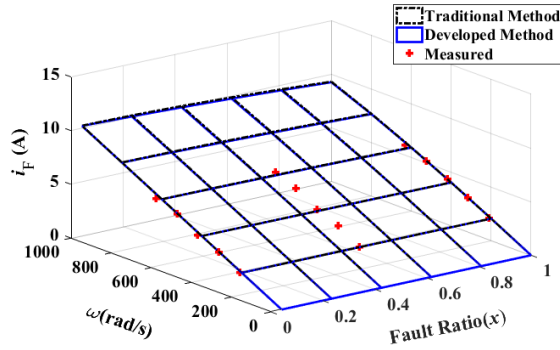

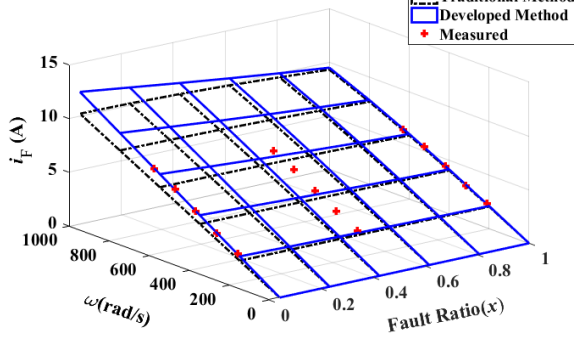Fig. 4. Amplitudes of predicted and measured fault currents *vs* x and ω_e.

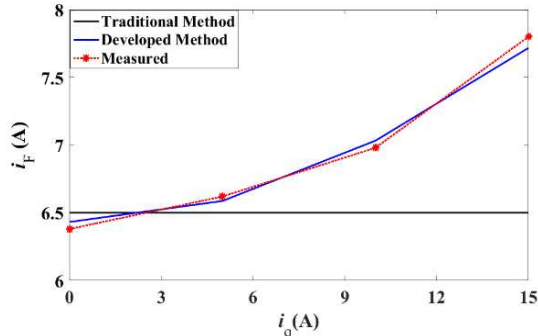Fig. 5. Amplitudes of predicted and measured fault currents. The load current is $i_d = 0$A and $i_a = 15$A.

Fig. 6 Amplitudes of predicted and measured fault currents *vs* i_q. $x = 1/24$ and $n = 1500$rpm ($\omega_e = 628$rad/s).

involving both simulation and measurement has been conducted in the following sections.

a. With No Load Current (i_d =0 and i_q =0)

If the load currents i_d and i_q are both set as 0A, the 1st term in (15) will no longer influence the fault current. As a result, the back-EMF in the short-circuited turns is regarded as the only voltage contributor to the fault current. In this case, the fault current has been calculated using (15) – proposed method, and it has been compared against (16) - conventional method, as seen in Fig. 4. It is found that the predicted fault current obtained by both the conventional model and the proposed model match well with the measured results. Fig. 4 also indicates that when ω_e increases, the amplitude of the fault current increases. This is due to the increased back-EMF in the short-circuited path. Within the maximum speed range, e.g., n=1500rpm (ω_e=628 rad/s), the amplitude of the fault current almost stays constant when x increases. This is because, in this speed range, the resistance plays a dominant role in the impedance calculation. For other cases where the maximum speed is even higher, the amplitude of the fault current will be changed when x changes. This can be predicted by both (15) and (16).

b. With Load Current (i_d = 0 and $i_q \neq$ 0)

In this section, the load current is set to be i_d =0 and $i_q \neq$ 0 to investigate the influence of i_q on the prediction of fault current obtained by the conventional and proposed methods. Under this condition, again using (15) and (16), the fault current has been calculated, as shown in Fig. 5. It is found from Fig. 5 that the fault current predicted by the developed method agrees well with the measured ones, proving its accuracy.

In order to further demonstrate the influence of i_q over the fault current, experiments and simulations with 4 different i_q such as 0A, 5A, 10A and 15A have been carried out. For these experiments and simulations, $x = 1/24$ and $n = 1500$rpm are maintained the same. Fig. 6 indicates that using the traditional method, the predicted fault current stays constant with different i_q. This differs from the measured results as it neglects the contribution of the load current to the fault current. When $i_q =$ 15A, the difference between the predicted fault current obtained by the traditional method and the measured one could be 1.2A, resulting in an error of almost 20%. If the developed method is adopted, only a slight error between the predicted results and the measured ones is observed, as shown in Fig. 6.

c. With Flux-Weakening Control ($i_d \neq$ 0)

It is well-established that the presence of a negative d-axis current (i_d) can reduce the total flux in the short-circuited path, leading to reduced short-circuit current. As a result, when ITSC fault is detected, an effective approach to mitigate the fault current is to introduce a negative i_d. This is consistent with the observation based on the 2nd term of (15), i.e., $\frac{K_{11}K_{34} - K_{31}K_{14}}{K_{11}}\left(E_{af}^2\right)$. However, in this paper, according to (15), it is found that i_d in the 1st term, i.e., $\frac{K_{31}}{K_{11}}\left(i_d^2 + i_q^2\right)$, regardless its sign, can potentially lead to an increase in the fault current. This is because as the absolute values of i_d and i_q increase, the phase current also increases. As a result, the fault current rises due to

the mutual inductances between the faulty turns and the remaining healthy windings (faulted and healthy phase). Obviously, the resultant impact of i_d on the resultant fault current will depend on the weightings of the 1st and 2nd terms of (15). To validate the impact of i_d on the fault current while excluding the influence of i_q, i_d was set to -10A and i_q was set
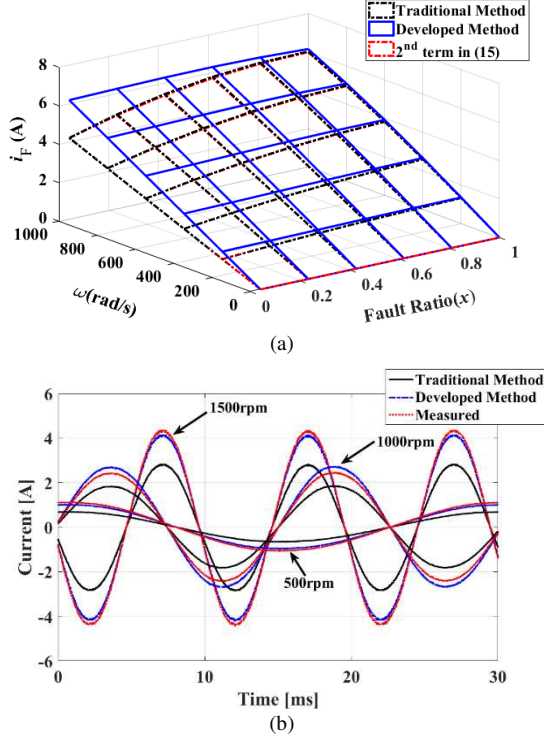

(a)

(b)

Fig. 7. (a) Amplitudes of predicted fault currents *vs* x and ω_e, and (b) measured and predicted fault currents with $x=1/24$. The load current is $i_d = -10A$ and $i_q = 0A$.
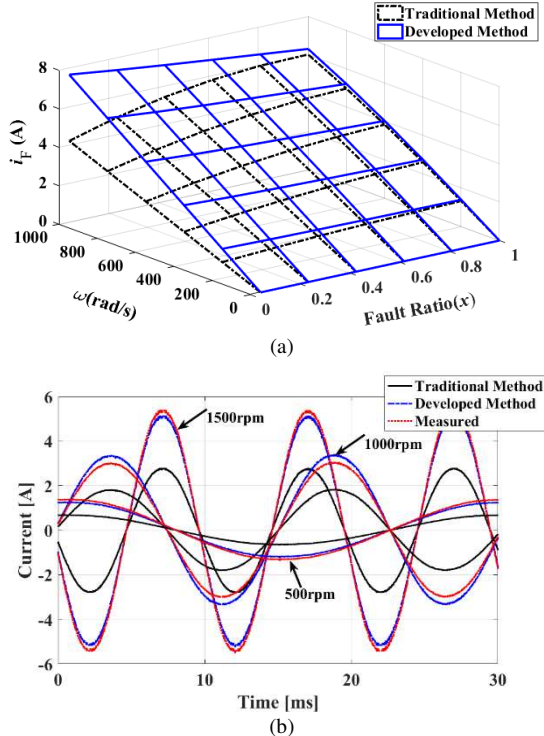

(a)

(b)

Fig. 8. (a) Amplitudes of predicted fault currents *vs* x and ω_e, and (b) measured and predicted results with $x=1/24$. The load current is $i_d = -10A$ and $i_q = 10A$.

to 0A. By comparing Fig. 4 and Fig. 7 (a), it is found that with a negative i_d injected, the fault current is actually reduced overall. However, the fault current predicted by the developed model is larger than that predicted by the conventional method (also considering the impact of i_d). This is because the developed model considers the contribution of i_d to the increase in the fault current. If this contribution is not considered, and only the 2nd term of (15) is taken into account, the difference in the fault current between the developed model and the traditional model is not significant, as seen in Fig. 7 (a). It is also found from Fig. 7 (a) that there is a significant difference in the predicted fault current between the two methods when the fault ratio is relatively low. This is because, at a lower fault ratio, the value of K_{31}/K_{11} [see Fig. 9 (a)] is larger, making the effect of the 1st term in (15) more pronounced. Therefore, only one turn being short-circuited is selected to experimentally verify the accuracy of this proposed fault model. It can be observed from Fig. 7 (b) that the predicted result by using developed model agrees well with the measured ones. Fig. 7 (b) also shows that the difference between the fault currents predicted by the conventional method and the measured ones could reach 1.2A, indicating an error of nearly 32%.

The second case investigated in this section is $i_d = -10A$ and $i_q = 10A$. In this scenario, the fault current has also been predicted by the traditional and proposed models, as seen in Fig. 8 (a). It can be seen that the fault current obtained by the proposed fault model is larger than that achieved from the traditional fault model. This is due to the fact that the developed model considers the influence of i_d and i_q on the increase in fault current. To verify the accuracy of the proposed model, tests have been conducted, as shown in Fig. 8 (b). It is found that the predicted results obtained from the developed method match well with the measured ones. Additionally, Fig. 8 (b) also demonstrates that the difference between the fault current predicted by the conventional method and the measured ones can reach 2.2A, indicating an error of approximately 45%. This further confirms the necessity of considering i_d and i_q in the fault current prediction.

d. Influence of Mutual-Inductances on Fault Current Prediction

Based on sections III.A.b and III.A.c, it is evident that when considering the load current, the predicted fault current from this proposed model is larger than that obtained from the traditional method. This discrepancy arises from the consideration of mutual inductances. It can be observed from (15) that the first contributor to the fault current is introduced by the mutual inductances between the faulted turns and the remaining healthy windings (faulted and healthy phase). If
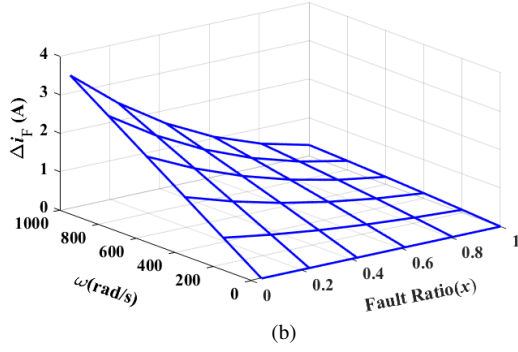

(a)

(b)
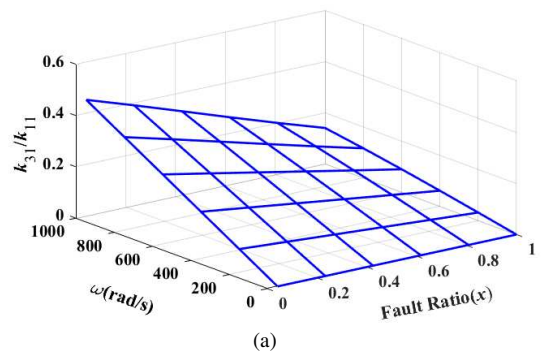
Fig. 9 (a) K_{31}/K_{11} in equation (15) vs x and ω_e. (b) amplitude difference between the fault currents calculated by the developed method and the traditional method. The load current is $i_d = -10A$ and $i_q = 10A$.

these mutual inductances are ignored, the matrix L in (2) will be updated as shown in (17). If so, K_{31}/K_{11} in (15) is equal to zero. From a broad perspective, one can define the K_{31}/K_{11} as a resultant mutual inductance between the faulted turns and remaining healthy windings (faulted and healthy phase). It can be founded from Fig. 9(a) that, if the fault ratio is kept constant (e.g., $x=1/24$) and with the speed (ω_e) increasing, K_{31}/K_{11} become larger. This leads to the differences between the faulted current predicted by the traditional method and proposed method becomes larger, as shown in Fig. 9 (b). However, when the speed is fixed, with an increase in fault ratio, this difference will be reduced [see Fig. 9 (b)]. This is because, with the increase in fault ratio, K_{31}/K_{11} will decrease as well [see Fig. 9(a)]. In addition, Fig. 6 further demonstrates the mutual inductance influence over the fault current. If these mutual inductances are neglected, the fault current remains unaffected, even in the presence of load current, as seen in Fig. 6.

$$L = \mathbf{diag}(L_{s11}, L_{s22}, L_{s33}, L_{s44}) \qquad (17)$$

B. Investigation of PWM Ripple Component in Fault Current

In the modern drive system, the PM machine is mainly controlled by the PWM inverter. Using Fast Fourier Transform (FFT) method, the PWM voltages output from the inverter can be decomposed as a series of sinusoidal signals of different frequencies and different amplitudes. These PWM voltage harmonics can be regarded as the input for the PM machine, and the PWM ripple current will be its output signal. The findings in [21] have shown that the PWM ripple components in the fault current can be much larger than that in the faulted phase current, especially with a small number of turns being short-circuited. Neglecting the PWM ripple component could lead to a serious underestimation of the fault current. As a result, this section will focus on the investigation of PWM ripple component in the fault current. In this section, the amplitudes of the fault current and faulted phase current refer to the amplitudes of their PWM ripple current.

To calculate the PWM ripple currents, (9) is still appliable.

Given the fact that the back-EMF in the short-circuited turns has no PWM harmonics, (9) can be replaced by (18). It is worth noting that A_1, B_1, A_2, B_2, A_3, B_3, C_1, D_1, C_2, and D_2 in (18) are functions of x and switching frequency.

$$\begin{bmatrix} i_{\alpha sh} \\ i_{\alpha ch} \\ i_{\beta sh} \\ i_{\beta ch} \\ i_{fsh} \\ i_{fch} \end{bmatrix} = \begin{bmatrix} A_1 & B_1 & 0 & 0 & C_1 & D_1 \\ -B_1 & A_1 & 0 & 0 & -D_1 & C_1 \\ 0 & 0 & A_2 & B_2 & 0 & 0 \\ 0 & 0 & -B_2 & A_2 & 0 & 0 \\ A_3 & B_3 & 0 & 0 & C_2 & D_2 \\ -B_3 & A_3 & 0 & 0 & -D_2 & C_2 \end{bmatrix} \begin{bmatrix} v_{\alpha sh} \\ v_{\alpha ch} \\ v_{\beta sh} \\ v_{\beta ch} \\ 0 \\ 0 \end{bmatrix} \qquad (18)$$

with

$$\begin{cases} \sqrt{i_{ash}^2 + i_{ach}^2} = i_{\alpha h} \\ \sqrt{i_{\beta sh}^2 + i_{\beta ch}^2} = i_{\beta h} \\ \sqrt{i_{fsh}^2 + i_{fch}^2} = i_{fh} \end{cases} \text{and} \begin{cases} \sqrt{v_{ash}^2 + v_{ach}^2} = v_{\alpha h} \\ \sqrt{v_{\beta sh}^2 + v_{\beta ch}^2} = v_{\beta h} \end{cases} \qquad (19)$$

where $i_{\alpha h}$, $i_{\beta h}$ and i_{fh} are the K [see (8)] value of α- and β-axis currents and fault current at switching frequency. $i_{\alpha sh}$, $i_{\beta sh}$ and i_{fsh}, and $i_{\alpha ch}$, $i_{\beta ch}$ and i_{fch} are F_s and F_c of $i_{\alpha h}$, $i_{\beta h}$ and i_{fh}, respectively. Similarly, $v_{\alpha h}$ and $v_{\beta h}$ are the K values of α- and β-axis voltage at switching frequency. $v_{\alpha sh}$, $v_{\beta sh}$ and $v_{\alpha ch}$, $v_{\beta ch}$ are F_s and F_c of the $v_{\alpha h}$ and $v_{\beta h}$, respectively.

Based on (18) and (19), the amplitudes of fault current and phase A current at switching frequency can be calculated, as seen in (20). However, it requires the amplitude of phase A voltage ($v_{\alpha h}$) in each PWM period, which is derived by decomposing the PWM voltage of phase A. The PWM voltage of phase A is determined by the difference between the PWM voltage of phase A (V_{dslA}) and the neutral point voltage (v_n), as seen in (3). It is known that V_{dslA} depends on the duty ratio of phase A, which in turn relies on the operation conditions of the PM machine, the adopted modulation strategy, and DC bus voltage. On the other hand, v_n depends on the duty ratio of each phase, fault ratio, DC bus voltage, and machine parameters, e.g., phase inductance, phase resistance, etc. Thus, predicting $v_{\alpha h}$ at each PWM period is challenging. However, the faulted phase current can be directly measured in practice. This enables the analysis of the amplitude of faulted phase current at the switching frequency. Using (21), which describes a ratio of the fault current amplitude over the faulted phase current at switching frequency, it is possible to indirectly predict the PWM ripple current in the short-circuited turns. In other words, (21) opens the possibility of assessing the unmeasurable PWM ripple current in the short-circuited turns.

$$\begin{cases} i_{\alpha h} = \sqrt{(A_1{}^2 + B_1{}^2)} v_{\alpha h} \\ i_{fh} = \sqrt{(A_3{}^2 + B_3{}^2)} v_{\alpha h} \end{cases} \qquad (20)$$

$$\frac{i_{fh}}{i_{\alpha h}} = \frac{\sqrt{(A_3{}^2 + B_3{}^2)}}{\sqrt{(A_1{}^2 + B_1{}^2)}} \qquad (21)$$

Based on (21), the ratio of the PWM ripple current in the short-circuited turns to that in the faulted phase can be calculated for different frequencies and fault ratios, as shown in Fig. 10. For the investigated machine, with 1 turn being short-circuited, the PWM ripple component in the fault current is about 23 times greater than that in the faulted phase. This further proves the necessity of considering the PWM ripple current in the short-circuited turns. With the increase in fault ratio, the ratio of i_F/i_a will decrease. This is because the
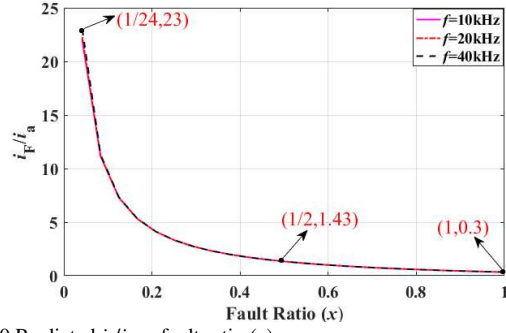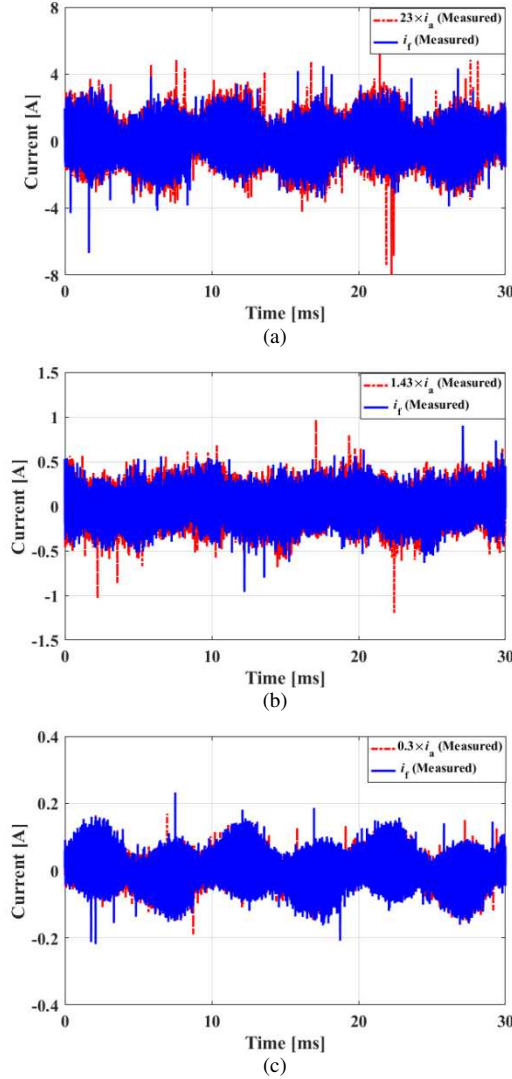
Fig. 10 Predicted i_F/i_a vs fault ratio (x).

(a)

(b)

(c)

Fig. 11 Measured PWM ripple component in i_F and i_a. (a) $x = 1/24$, (b) $x = 1/2$, and (c) $x = 1$. $n = 1500$rpm, $f=20$kHz, and $i_d = 0$A and $i_q = 2$A.

impedance of the short-circuited turns increases, whilst it reduces in the faulted phase. The findings in [23] demonstrated an inverse correlation between the impedance of the phase current and the amplitude of the PWM ripple component. It is also found from Fig. 10 that the ratio of i_F/i_a is independent of the switching frequency. This can be attributed to the fact that as the switching frequency increases, the PWM ripple components in the faulted phase current and in the fault current decrease simultaneously [24].

In order to further demonstrate the relationship presented in Fig. 10, the PWM ripple component is extracted from the measured faulted phase current (i_a) and fault current (i_f) under different fault ratios (x). Fig. 11 illustrates the accuracy of the proposed relationship between the PWM ripple component in the faulted current and the faulted phase current, as described in (21). It should be noted that this relationship only depends on machine parameters and fault ratio. Consequently, if machine parameters and fault ratio are unchanged, the ratio (i_F/i_a) will remain constant under different operational scenarios.

C. Fault Current Prediction Considering Fundamental and PWM Ripple Components

By utilizing the measured faulted phase current i_a, as show in Fig. 12 (I) (a), it is easy to determine its PWM ripple component, as shown in Fig. 12 (I) (b), which can then be utilized to predict the PWM ripple component in the fault current using (21), as shown in Fig. 12 (I) (c). In addition, (15) can be employed to calculate the magnitude of the fundamental
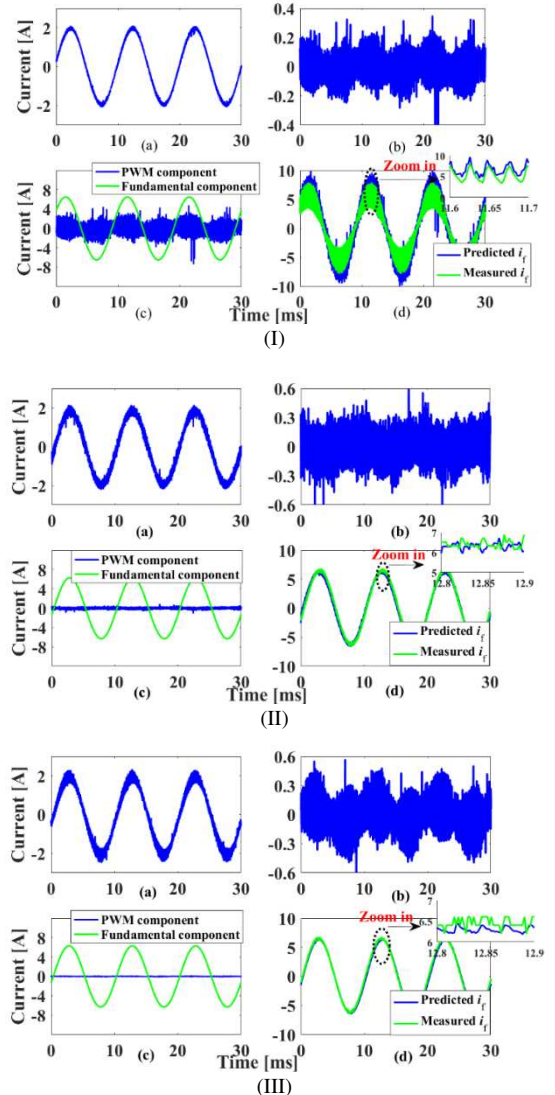

(I)

(II)

(III)

Fig. 12 (I) $x = 1/24$, (II) $x = 1/2$, and (III) $x = 1$. (a) measured i_a, (b) PWM ripple current in measured i_a, (c) predicted PWM ripple component and fundamental component in i_f, and (d) predicted and measured i_f. $n = 1500$rpm, $i_d = 0$A and $i_q = 2$A.

component of the fault current, as shown in Fig. 12 (I) (c). Consequently, adding the PWM ripple and the fundamental components together, the fault current can be predicted, as shown in Fig. 12 (I) (d). It can be observed from Fig. 12 that with different fault ratios, the predicted fault currents closely match with the measured ones. Therefore, it can be concluded that by employing (15) and (21), and using the measured faulted phase current, the fault current, which is unmeasurable in practice, can be accurately predicted. Additionally, with an increase in x, the PWM ripple component in the faulted phase current also increases due to the decrease in impedance in the faulted phase. This behavior is opposite to that of the fault current.

IV. CONCLUSION

In this article, a novel analytical model in α- and β-axis reference frame has been developed. Such model can be used to derive a generic mathematical expression of the amplitude of the fault current. The investigation in this article shows that compared with the commonly used fault current prediction method in literature, the proposed approach is much more accurate. This improved accuracy can be attributed to the inclusion and proper consideration of other factors that contribute to the fault current calculation, such as (i) mutual inductances between the faulty turns and the remaining healthy windings (both faulty and healthy phases) and (ii) load current. In addition, this article establishes a relationship between the PWM ripple current in the short-circuited turns and the corresponding PWM ripple current in the faulted phase. This correlation enables the accurate prediction of the fault current by considering both the fundamental component and the PWM ripple component simultaneously. A series of experiments have been carried out to validate the proposed fault current prediction method.

APPENDIX A

A full rank matrix is defined as $\boldsymbol{M}$ in (A1) and its inverse matrix can be obtained. Meanwhile, the relevant linear transformation is described by (A2).

$$\boldsymbol{M} = \frac{1}{3}\begin{bmatrix} 2 & -1 & -1 & 0 \\ 0 & \sqrt{3} & -\sqrt{3} & 0 \\ 0 & 0 & 0 & 3 \\ 1 & 1 & 1 & 0 \end{bmatrix} \tag{A1}$$

$$\begin{bmatrix} i_\alpha \\ i_\beta \\ i_f \\ i_0 \end{bmatrix} = \boldsymbol{M}\begin{bmatrix} i_a \\ i_b \\ i_c \\ i_f \end{bmatrix} \text{ and } \begin{bmatrix} v_\alpha \\ v_\beta \\ v_f \\ v_0 \end{bmatrix} = \boldsymbol{M}\begin{bmatrix} v_{Adsl} - e_{ah} \\ v_{Bdsl} - e_b \\ v_{Cdsl} - e_c \\ -e_{af} \end{bmatrix} \tag{A2}$$

where i_α, i_β, i_f and i_0 denote the new currents converted from i_a, i_b, i_c, and i_f using matrix $\boldsymbol{M}$. v_α, v_β, v_f and v_0 are the voltages transformed from the PWM voltage and back-EMF using matrix $\boldsymbol{M}$.

By substituting (A2) into (4), (A3) is obtained. Furthermore, both sides of (A3) are multiplied simultaneously by matrix $\boldsymbol{M}$, leading to (A4). Then, the product of matrices in front of the current and voltage vectors can be achieved, as illustrated by (A5).

$$\boldsymbol{PLM}^{-1}\frac{d}{dt}\begin{bmatrix} i_\alpha \\ i_\beta \\ i_f \\ i_0 \end{bmatrix} = -\boldsymbol{PRM}^{-1}\begin{bmatrix} i_\alpha \\ i_\beta \\ i_f \\ i_0 \end{bmatrix} + \boldsymbol{PM}^{-1}\begin{bmatrix} v_\alpha \\ v_\beta \\ v_f \\ v_0 \end{bmatrix} \tag{A3}$$

$$\boldsymbol{MPLM}^{-1}\frac{d}{dt}\begin{bmatrix} i_\alpha \\ i_\beta \\ i_f \\ i_0 \end{bmatrix} = -\boldsymbol{MPRM}^{-1}\begin{bmatrix} i_\alpha \\ i_\beta \\ i_f \\ i_0 \end{bmatrix} + \boldsymbol{MPM}^{-1}\begin{bmatrix} v_\alpha \\ v_\beta \\ v_f \\ v_0 \end{bmatrix} \tag{A4}$$

with

$$\boldsymbol{MPLM}^{-1} = \begin{bmatrix} \boldsymbol{L}_{3\times3} & \boldsymbol{L}_{3\times1} \\ \boldsymbol{0}_{1\times3} & 0 \end{bmatrix}, -\boldsymbol{MPRM}^{-1} = \begin{bmatrix} \boldsymbol{R}_{3\times3} & \boldsymbol{R}_{3\times1} \\ \boldsymbol{0}_{1\times3} & 0 \end{bmatrix}$$
$$\text{and } \boldsymbol{MPM}^{-1} = \begin{bmatrix} \boldsymbol{E}_{3\times3} & \boldsymbol{0}_{3\times1} \\ \boldsymbol{0}_{1\times3} & 0 \end{bmatrix} \tag{A5}$$

where $\boldsymbol{L}_{3\times3}$ is a 3×3 inductance matrix. It is converted by linear transformation from the matrix $\boldsymbol{L}$, the previously defined matrix $\boldsymbol{M}$ and its inverse matrix $\boldsymbol{M}^{-1}$, and the matrix $\boldsymbol{P}$. $\boldsymbol{L}_{3\times1}$ is a 3×1 inductance matrix, which is extracted from the 4th column of the product of matrices $\boldsymbol{M}$, $\boldsymbol{P}$, $\boldsymbol{L}$ and $\boldsymbol{M}^{-1}$. $\boldsymbol{R}_{3\times3}$ is a 3×3 resistance matrix, which is the first three rows and columns of the product of matrices $\boldsymbol{M}$, $\boldsymbol{P}$, $\boldsymbol{R}$ and $\boldsymbol{M}^{-1}$. $\boldsymbol{R}_{3\times1}$ is a 3×1 resistance matrix. $\boldsymbol{E}_{3\times3}$ is a 3×3 identity matrix. $\boldsymbol{0}_{1\times3}$ and $\boldsymbol{0}_{3\times1}$ are matrices with a dimension of 1×3 and 3×1, respectively, and the elements in these two matrices are all equal to zero.

APPENDIX B

For a first-order linear system with sinusoidal input, the expression can be given as (B1).

$$\frac{d}{dt}x(t) = a_1 x(t) + b_1 u(t) \tag{B1}$$

with

$$u_1(t) = \begin{bmatrix} \sin(\omega t) \\ \cos(\omega t) \end{bmatrix}^T \begin{bmatrix} u_s \\ u_c \end{bmatrix}, x(t) = \begin{bmatrix} \sin(\omega t) \\ \cos(\omega t) \end{bmatrix}^T \begin{bmatrix} x_s \\ x_c \end{bmatrix} \tag{B2}$$

where $x(t)$ is the state variable and $u(t)$ is the input signal. x_s, x_c and u_s, u_c represent the values of F_s and F_c, respectively. For $x(t)$ and $u(t)$, a_1 and b_1 are their coefficients.

With (B2), (B1) can be derived as (B3).

$$\frac{d}{dt}\begin{bmatrix} x_s \\ x_c \end{bmatrix} = \begin{bmatrix} a_1 & \omega \\ -\omega & a_1 \end{bmatrix}\begin{bmatrix} x_s \\ x_c \end{bmatrix} + \begin{bmatrix} b_1 & 0 \\ 0 & b_1 \end{bmatrix}\begin{bmatrix} u_s \\ u_c \end{bmatrix} \tag{B3}$$

Since x_s and x_c are constants, (B3) can be further expressed as (B4).

$$[\boldsymbol{x}_{sc}] = -\boldsymbol{A}^{-1}\boldsymbol{B} \tag{B4}$$

with

$$\boldsymbol{A} = \begin{bmatrix} a_1 & \omega \\ -\omega & a_1 \end{bmatrix} \text{ and } \boldsymbol{B} = \begin{bmatrix} b_1 & 0 \\ 0 & b_1 \end{bmatrix} \tag{B5}$$

where $\boldsymbol{x}_{sc}$ is a 2×1 matrix consisting of x_s and x_c.

If a multi-order system is considered, expressed as (B6), similar derivation process for first-order system can be applied. As a result, the values of F_s and F_c for each sinusoidal signals including the inputs and state variables can be derived as (B7).

$$\frac{d}{dt}\begin{bmatrix} x_1 \\ x_2 \\ \dots \\ x_n \end{bmatrix} = \begin{bmatrix} a_{11} & a_{12} & \dots & a_{1n} \\ a_{21} & a_{22} & \dots & a_{2n} \\ \dots & \dots & \dots & \dots \\ a_{n1} & a_{n2} & \dots & a_{nn} \end{bmatrix}\begin{bmatrix} x_1 \\ x_2 \\ \dots \\ x_n \end{bmatrix} + \begin{bmatrix} b_{11} & b_{12} & \dots & b_{1n} \\ b_{21} & b_{22} & \dots & b_{2n} \\ \dots & \dots & \dots & \dots \\ b_{n1} & b_{n2} & \dots & b_{nn} \end{bmatrix} \tag{B6}$$

$$\begin{bmatrix} x_{1sc} \\ x_{2sc} \\ \dots \\ x_{nsc} \end{bmatrix} = -\begin{bmatrix} a_{11}\times\boldsymbol{I}_2 - \boldsymbol{M}_\omega & a_{12}\times\boldsymbol{I}_2 & \dots & a_{1n}\times\boldsymbol{I}_2 \\ a_{21}\times\boldsymbol{I}_2 & a_{22}\times\boldsymbol{I}_2 - \boldsymbol{M}_\omega & \dots & a_{2n}\times\boldsymbol{I}_2 \\ \dots & \dots & \dots & \dots \\ a_{n1}\times\boldsymbol{I}_2 & a_{n2}\times\boldsymbol{I}_2 & \dots & a_{nn}\times\boldsymbol{I}_2 - \boldsymbol{M}_\omega \end{bmatrix}^{-1}\begin{bmatrix} b_{11}\times\boldsymbol{I}_2 & b_{12}\times\boldsymbol{I}_2 & \dots & b_{1n}\times\boldsymbol{I}_2 \\ b_{21}\times\boldsymbol{I}_2 & b_{22}\times\boldsymbol{I}_2 & \dots & b_{2n}\times\boldsymbol{I}_2 \\ \dots & \dots & \dots & \dots \\ b_{n1}\times\boldsymbol{I}_2 & b_{n2}\times\boldsymbol{I}_2 & \dots & b_{nn}\times\boldsymbol{I}_2 \end{bmatrix}\begin{bmatrix} u_{1dq} \\ u_{2dq} \\ \dots \\ u_{ndq} \end{bmatrix} \tag{B7}$$

$$\boldsymbol{M_\omega} = \begin{bmatrix} 0 & -\omega \\ \omega & 0 \end{bmatrix} \text{ and } \boldsymbol{I_2} = \begin{bmatrix} 1 & 0 \\ 0 & 1 \end{bmatrix} \tag{B8}$$

where x_1, x_2… and x_n are the state variables and u_1, u_2… and u_n are the input signals. $\boldsymbol{x_{1sc}}$, $\boldsymbol{x_{2sc}}$… and $\boldsymbol{x_{nsc}}$ represent the values of F_s and F_c of x_1, x_2…and x_n, and each of them is a 2×1 matrix consisting of x_{is} and x_{ic}. Similarly, $\boldsymbol{u_{1sc}}$, $\boldsymbol{u_{2sc}}$… and $\boldsymbol{u_{nsc}}$ represent the values of F_s and F_c of u_1, u_2…and u_n, and each of them is a 2×1 matrix consisting of u_{is} and u_{ic}. $a_{11} \dots a_{nn}$, and $b_{11} \dots b_{nn}$ are the coefficients, $\boldsymbol{M_\omega}$ is a 2×2 matrix , and $\boldsymbol{I_2}$ is a 2×2 identity matrix.

$$A_1 = 12R\left[\omega^2 x\left(9L_m^2 - 8L_mL_lx^2 + 24L_mL_lx - 4L_l^2x^2 + 12L_l^2x\right) + R^2(12 - 4x)\right]/DEN \tag{B9}$$

$$\begin{aligned} B_1 = 12\omega[&\omega^2x^2\left(9L_m^3 + 8L_m^2L_lx^2 - 20L_m^2L_lx + 39L_m^2L_l \right. \\ &\left. + 12L_mL_l^2x^2 - 28L_mL_l^2x + 42L_mL_l^2 + 4L_l^3x^2 \right. \\ &\left. - 8L_l^3x + 12L_l^3\right) \\ &+ Rx(4L_mRx - 12L_mR + 4L_lRx - 8L_lR) \\ &+ R^2(18L_m + 12L_l)]/DEN \end{aligned} \tag{B10}$$

$$A_2 = \frac{4R}{\omega^2(2L_l + 3L_m)^2 + 4R^2} \tag{B11}$$

$$B_2 = \frac{2\omega(2L_l + 3L_m)}{\omega^2(2L_l + 3L_m)^2 + 4R^2} \tag{B12}$$

$$A_3 = 12L_mR\omega^2(2x - 3)(9L_m + 6L_l + 2L_lx)/DEN \tag{B13}$$

$$\begin{aligned} B_3 = 6L_m\omega(2x - 3)[&\omega^2x\left(9L_m^2 + 30L_mL_l + 12L_l^2\right) \\ &+ \omega^2x^2\left(8L_mL_lx - 20L_mL_l + 4L_l^2x - 8L_l^2\right) \\ &+ R^2(4x - 12)]/DEN \end{aligned} \tag{B14}$$

$$C_1 = 8L_mR(2x - 3)\omega^2(9L_m + 6L_l + 2L_lx)/DEN \tag{B15}$$

$$\begin{aligned} D_1 = 4L_m\omega(2x - 3)[&\omega^2x\left(9L_m^2 + 30L_mL_l + 12L_l^2\right) \\ &+ \omega^2x^2\left(8L_mL_lx - 20L_mL_l + 4L_l^2x - 8L_l^2\right) \\ &+ R^2(4x - 12)]/DEN \end{aligned} \tag{B16}$$

$$\begin{aligned} C_2 = 8\frac{R}{x}[&\omega^2x^2\left(27L_m^2 + 8L_mL_lx^2 - 40L_mL_lx + 108L_mL_l\right) \\ &+ \omega^2\left(81L_m^2 + 108L_mL_l + 36L_l^2\right) \\ &- 81\omega^2x\left(81L_m^2 + 144L_mL_l + 48L_l^2\right) \\ &+ 4R^2(x - 3)^2]/DEN \end{aligned} \tag{B17}$$

$$\begin{aligned} D_2 = 4\omega[&\omega^2x^2\left(18L_m^3 + 16L_m^2L_lx^2 - 88L_m^2L_lx + 270L_m^2L_l \right. \\ &\left. + 24L_mL_l^2x^2 - 112L_mL_l^2x + 296L_mL_l^2 \right. \\ &\left. + 8L_l^3x^2 - 32L_l^3x + 80L_l^3\right) \\ &+ \omega^2\left(324L_m^2L_l - 54L_m^3x + 81L_m^3 \right. \\ &\left. - 396L_m^2L_lx - 384L_mL_l^2x + 288L_mL_l^2 \right. \\ &\left. - 96L_l^3x + 72L_l^3\right) \\ &+ R^2(8L_mx^2 - 48L_mx + 72L_m + 8L_lx^2 \\ &- 48L_lx + 72L_l)]/DEN \end{aligned} \tag{B18}$$

with

$$\begin{aligned} DEN = \omega^4x^2[&81L_m^4 \\ &+ L_l^4(16x^4 - 64x^3 + 160x^2 - 192x + 144) \\ &+ L_m^3L_l(144x^2 - 360x + 540) \\ &+ L_mL_l^3(64x^4 - 288x^3 + 752x^2 - 960x \\ &+ 720) \\ &+ L_m^2L_l^2(64x^4 - 320x^3 + 952x^2 - 1344x \\ &+ 1116)] \\ &+ R^2\omega^2[L_m^2(72x^2 - 216x + 324) \\ &+ L_l^2(32x^4 - 160x^3 + 304x^2 - 192x \\ &+ 144) \\ &+ L_mL_l(64x^4 - 352x^3 + 720x^2 - 576x \\ &+ 432)] + R^4(16x^2 - 96x + 144) \end{aligned} \tag{B19}$$

where L_m is the self-magnetizing inductance, L_l is the phase leakage inductance and R is the phase resistance.

REFERENCES

[1] A. Emadi, Y. J. Lee, and K. Rajashekara, "Power electronics and motor drives in electric, hybrid electric, and plug-in hybrid electric vehicles," *IEEE Trans. Power Electron.*, vol. 55, no. 6, pp. 2237-2245, Jun. 2008.

[2] F. Briz, M. W. Degner, A. Zamarron and J. M. Guerrero, "Online stator winding fault diagnosis in inverter-fed AC machines using high-frequency signal injection," *IEEE Trans. Ind. Appl.,* vol. 39, no. 4, pp. 1109-1117, Jul.-Aug. 2003.

[3] J. Yang, J. Cho, S. B. Lee, J. Y. Yoo and H. D. Kim, "An advanced stator winding insulation quality assessment technique for Inverter-Fed Machines," *IEEE Trans. Ind. Appl.,*, vol. 44, no. 2, pp. 555-564, Mar.-Apr. 2008.

[4] M. F. Shaikh, H. Lee, B. Battulga, S. B. Lee, and G. C. Stone, "Offline Common-Mode Voltage Based Inverter-Embedded Groundwall Insulation Testing for Motors," *2022 International Conference on Electrical Machines (ICEM)*, Valencia, Spain, 2022, pp. 1823-1829.

[5] J. Hang, W. Sun, Q. Hu, X. Ren, and S. Ding, "Integration of interturn fault diagnosis and fault-tolerant control for PMSM drive system," *IEEE Trans. Transp. Electrif.,* vol. 8, no. 2, pp. 2825-2835, Jun. 2022.

[6] P. Zhang, K. Li, S. Yu, and D. Yu, "A novel fault diagnosis technique of interturn short-circuit fault for SRM in current chopper mode," *IEEE Trans. Ind. Electron.*, vol. 69, no. 3, pp. 3037-3046, Mar. 2022.

[7] İ. Şahin and O. Keysan, "Model predictive controller utilized as an observer for inter-turn short circuit detection in induction motors," *IEEE Trans. Energy Convers.*, vol. 36, no. 2, pp. 1449-1458, Jun. 2021.

[8] Y. Fu, Z. Ren, S. Wei, Y. Xu, and F. Li, "Using flux linkage difference vector in early inter-turn short circuit detection for the windings of offshore wind DFIGs," *IEEE Trans. Energy Convers.*, vol. 36, no. 4, pp. 3007-3015, Dec. 2021.

[9] B. Wang, J. B. Wang, A. Griffo, and W. Hua, "Effective turn fault mitigation by creating zero sequence current path for a triple redundant 3× 3-phase PMA SynRM," *IEEE Trans. Power. Electron.*, vol. 34, no. 11, pp. 11080-11089, Nov. 2019.

[10] Y. Xu, Z. Zhang, Y. Jiang, J. Huang, and W. Jiang, "Numerical analysis of turn-to-turn short circuit current mitigation for concentrated winding permanent magnet machines with series and parallel connected windings," *IEEE Trans. Ind. Electron.*, vol. 67, no. 11, pp. 9101-9111, Nov. 2020.

[11] G. Du, W. Ye, Y. Zhang, L. Wang, T. Pu, and N. Huang, "Comprehensive analysis of the AC copper loss for high speed PM machine with form-wound windings," *IEEE Access.,* vol. 10, pp. 9036-9047, 2022.

[12] Y. Qi, M. Zafarani, V. Gurusamy, and B. Akin, "Advanced severity monitoring of interturn short circuit faults in PMSMs," *IEEE Trans. Transp. Electrif.,* vol. 5, no. 2, pp. 395-404, Jun. 2019.

[13] Z. T. Mei, G. J. Li, Z. Q. Zhu, R. Clark, A. Thomas, and Z. Azar, "Scaling effect on inter-turn short-circuit fault of PM machines for wind power application," *IEEE Trans. Ind. Appl.,* vol. 59, no. 1, pp. 789-800, Jan.-Feb. 2023.

[14] J. Zhao, X. Guan, C. Li, Q. Mou, and Z. Chen, "Comprehensive evaluation of inter-turn short circuit faults in pmsm used for electric vehicles," *IEEE Trans. Intell. Transp. Syst.,* vol. 22, no. 1, pp. 611-621, Jan. 2021.

[15] R. Hu, J. Wang, A. R. Mills, E. Chong, and Z. Sun, "Current-residual-based stator interturn fault detection in permanent magnet machines," *IEEE Trans. Ind. Electron.*, vol. 68, no. 1, pp. 59-69, Jan. 2021.

[16] J. G. Cintron-Rivera, S. N. Foster, and E. Strangas, "Mitigation of turn-to-turn faults in fault tolerant permanent magnet synchronous motors," *IEEE Trans. Energy Convers.*, vol. 30, no. 2, pp. 465-475, Jun. 2015.

[17] F. Wu, P. Zheng, and T. M. Jahns, "Analytical modeling of interturn short circuit for multiphase fault-tolerant PM machines with fractional slot concentrated windings," *IEEE Trans. Ind. Appl.,* vol. 53, no. 3, pp. 1994-2006, May.-Jun. 2017.

[18] B. Gu, J. H. Choi, and I. Jung, "Development and analysis of interturn short fault model of PMSMs with series and parallel winding connections," *IEEE Trans. Power. Electron.*, vol. 29, no. 4, pp. 2016-2026, Apr. 2014.

[19] I. Jeong, B. J. Hyon, and K. Nam, "Dynamic modeling and control for SPMSMs with internal turn short fault," *IEEE Trans. Power. Electron.*, vol. 28, no. 7, pp. 3495-3508, Jul. 2013.

[20] K. H. Baruti, C. Li, F. Erturk, and B. Akin, "Online stator inter-turn short circuit estimation and fault management in permanent magnet motors," *IEEE Trans. Energy Convers.*, vol. 38, no. 2, pp. 1016-1027, Jun. 2023.

[21] Y. Qin, G. J. Li, C. Jia, and P. McKeever, "PWM voltage-based Modeling for PM machines with inter-turn short circuit fault considering the effect of drives," *IEEE Trans. Ind. Electron.*, vol. 70, no. 11, pp. 10981-10991, Nov. 2023.

[22] J. Hang, J. Zhang, M. Cheng, and J. Huang, "Online interturn fault diagnosis of permanent magnet synchronous machine using zero-sequence components," *IEEE Trans. Power. Electron.*, vol. 30, no. 12, pp. 6731-6741, Dec. 2015.

[23] L. Chang and T. M. Jahns, "Prediction and evaluation of PWM-induced current ripple in IPM machines incorporating slotting, saturation, and cross-coupling effects," *IEEE Trans. Ind. Appl.,* vol. 54, no. 6, pp. 6015-6026, Nov.-Dec. 2018.

[24] Y. Qin, G. J. Li, C. Jia, and P. McKeever, "Investigation of inter-turn short-circuit fault of PM machines using PWM voltage-based modeling," *IEEE Trans. Transp. Electrif.,* Early Access.